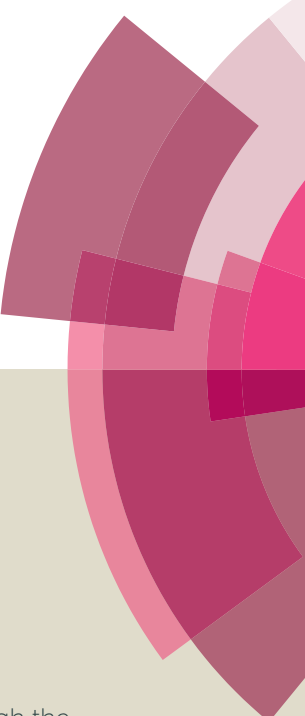
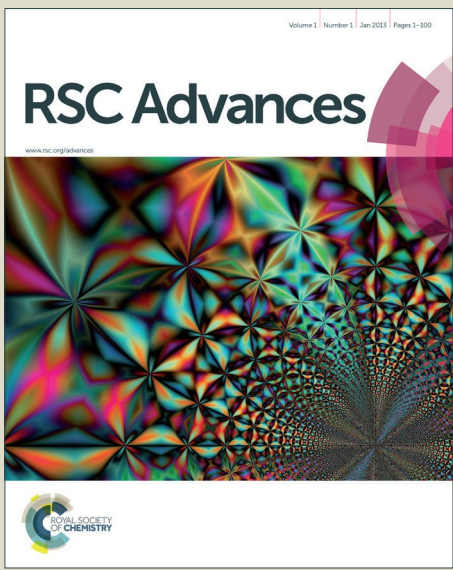


RSC Advances



This article can be cited before page numbers have been issued, to do this please use: Z. Liu, R. Yu, Y. Dong, W. Li and W. Zhou, *RSC Adv.*, 2016, DOI: 10.1039/C6RA15245G.



This is an Accepted Manuscript, which has been through the Royal Society of Chemistry peer review process and has been accepted for publication.

Accepted Manuscripts are published online shortly after acceptance, before technical editing, formatting and proof reading. Using this free service, authors can make their results available to the community, in citable form, before we publish the edited article. This Accepted Manuscript will be replaced by the edited, formatted and paginated article as soon as this is available.

You can find more information about Accepted Manuscripts in the [Information for Authors](#).

Please note that technical editing may introduce minor changes to the text and/or graphics, which may alter content. The journal's standard [Terms & Conditions](#) and the [Ethical guidelines](#) still apply. In no event shall the Royal Society of Chemistry be held responsible for any errors or omissions in this Accepted Manuscript or any consequences arising from the use of any information it contains.



Journal Name

ARTICLE

Preparation of α -Fe₂O₃ hollow spheres, nanotubes, nanoplates and nanorings as high efficient Cr(VI) adsorbents

Received 00th January 20xx,
Accepted 00th January 20xx

DOI: 10.1039/x0xx00000x

www.rsc.org/

Zhong Liu,^a Ruitao Yu,^b Yaping Dong,^a Wu Li*,^a Wuzong Zhou*,^c

Abstract: α -Fe₂O₃ nanoparticle with different morphologies, such as hollow spheres, nanotubes with limited {0001} plane exposed, nanoplates and nanorings with the {0001} plane predominantly exposed, have been synthesised by using NaH₂PO₄ and urea in a facile hydrothermal method. The mechanism of the morphology evolution from hollow sphere to nanoring has been investigated. It is proposed that the polymerisation of Fe³⁺/H₂PO₄⁻ plays an important role in the formation of these morphologies. The adsorption of Cr (VI) from aqueous solution onto these α -Fe₂O₃ nanoparticles showed that the α -Fe₂O₃ with nanoring morphology has the highest removal efficiency, and the adsorption capacity reached to 16.9 mg/g. These results indicate that the adsorption mechanism of Cr (VI) onto hematite nanoparticles is a chemisorption process through doubly and triply coordinated hydroxyl groups on the outer surface of α -Fe₂O₃.

Introduction

The contamination of water bodies caused by heavy metals is a serious environmental problem because of their toxicity to many life forms.¹ One of the common hazardous ions is Cr (VI) which usually occurs as highly soluble and toxic chromate anions (HCrO₄⁻ or Cr₂O₇²⁻), both being suspected carcinogens and mutagens. Various kinds of methods have been carried out for Cr (VI) ion removal such as precipitation, reverse osmosis, solvent extraction and electrolysis, biological treatment, ion-exchange processes, and adsorption.² Among them, the adsorption technique has advantages of high efficiency, cost effectiveness and environment-friendly.³ During the past decade, many types of adsorbents have been studied for their Cr(VI) removal effectiveness, including activated carbons, metal oxides, polymeric adsorbents, and even certain types of bio-sorbents.⁴ Among them, hematite (α -Fe₂O₃) has attracted a great interest owing to its effective performance, natural abundance, low cost and environmental safety.⁵

Some studies have shown that α -Fe₂O₃ has a good capacity for Cr (VI) adsorption in aqueous solution. Cao *et al.* prepared flower-like α -Fe₂O₃ nanostructures that have a high capacity for Cr(VI) adsorption.⁶ Han *et al.* prepared α -Fe₂O₃ with a porous structure that can rapidly adsorb Cr (VI) ions in wastewater at room temperature.⁷ Liu *et al.* obtained porous α -Fe₂O₃ nanostructures with different morphologies exhibited excellent Cr(VI) removal capacity and a fast adsorption rate in a wide

range of pH.⁸ Besides this, the adsorption ability and mechanism on different exposed planes of α -Fe₂O₃ have been partly calculated. Yin and Ellis revealed H₂CrO₄ adsorption to α -Fe₂O₃ {1102} surface plane by strong H-bonding.⁹ Huang *et al.* systematically investigated Cr(VI) on the hematite nanorods, and concluded that Cr(VI) species were adsorbed on the {0001} and {1120} planes in inner-sphere monodentate mononuclear and bidentate binuclear configurations.¹⁰ However, our knowledge of the morphology control of hematite crystals and the mechanism of Cr(VI) adsorption on the different surfaces of α -Fe₂O₃ is still very limited.

In the present work, with presence of NaH₂PO₄ and urea, the α -Fe₂O₃ nanoparticles with different morphologies, such as hollow spheres, nanotubes, nanoplates and nanorings, are successfully synthesised via a facile hydrothermal method. These α -Fe₂O₃ nanoparticles have good dispersion without using any substrates and show different exposed crystal planes. The microstructural studies of the specimens under different synthetic conditions lead to establishment of a new non-classical crystal growth route. The ability to remove Cr(VI) using these as-synthesised α -Fe₂O₃ is examined, and the possible mechanism of adsorption of Cr(VI) on the crystal surface is deduced.

Experimental

All chemicals were in analytical purity, and used without further purification. A typical experiment to prepare α -Fe₂O₃ is as follows: required amounts of NaH₂PO₄ and urea were added under stirring to 80 mL aqueous solution of 23 mmol/L of FeCl₃. The solution was subsequently sealed in a 100 mL autoclave, and maintained at 220 °C for 24 h. The autoclave was then cooled down to room temperature gradually. The red precipitates were collected by centrifugation, and washed with deionised water and ethanol for three times, and finally dried in

^a Qinghai Institute of Salt Lakes, Chinese Academy of Sciences, Xining 810008, China, email: liwu2016@126.com

^b Northwest Plateau of Biology Institute, Chinese Academy of Sciences, Xining 810008, China

^c EaStChem, School of Chemistry, University of St Andrews, St Andrews, KY16 9ST, UK. email: wzhou@st-andrews.ac.uk

† Electronic Supplementary Information (ESI) available: More SEM images, XPS, Cr(VI)-adsorption capacities. See DOI: 10.1039/x0xx00000x

ARTICLE

a desiccator at 60 °C for 12 h. The concentrations of NaH₂PO₄ and urea used in the synthesis are listed in Table 1. Powder X-ray diffraction (XRD) was performed on a PANalytical Empyrean diffractometer using Cu K α radiation. The morphology of the samples were observed using scanning electron microscopy (SEM, LEO 1530VP). The microstructures and crystal structures of the particles were investigated using transmission electron microscopy (TEM) and high resolution TEM (HRTEM) on a JEOL JEM-2011FEF microscope. X-ray photoelectron spectroscopy (XPS) analysis was performed on a PHI 5300x multitechnique system with a Mg-K α X-ray source (Perkin-Elmer Physical Electronics). The nitrogen adsorption-desorption isotherms were obtained using a JW-BK specific surface area instrument (Beijing, China) and the specific surface areas were calculated using the Brunauer-Emmett-Teller (BET) method.

Table 1: Compositions of the synthetic solutions

Sample number	FeCl ₃ (mmol/L)	PO ₄ ³⁻ (mmol/L)	Urea(mmol/L)
S1	23.00	0	0.50
S2	23.00	1.0	1.0
S3	23.00	2.50	2.50
S4	23.00	4.00	4.00

Batch adsorption studies were performed by mixing 0.12g of the sample with 50 mL of Cr(VI) solution of various concentrations in a 150 mL conical flask with a shaking speed of 150 rpm. The adsorption experiments were carried out at the room temperature, and were conducted at the initial pH of the Cr(VI) solution without adjustment unless otherwise specified. To study the effect of pH, the pH values of the Cr(VI) solution were adjusted from 3 to 11 using 1.0 mol/L HCl and 1.0 mol/L NaOH solutions. The desorption process of Cr(VI) from the samples took place in 50 ml of 0.01M NaOH to reach Cr(VI) desorption equilibrium in 24 h. The concentrations of Cr(VI) were determined using a GBC-908 Atomic Absorption Spectrometer (GBC Scientific Equipment Pty Ltd.). The removal efficiency (E%) and the equilibrium adsorption capacity (q_e , mg/g) were calculated using eqn (1) and (2), respectively:

$$E(\%) = \frac{C_0 - C_t}{C_0} \times 100\% \quad (1)$$

$$q_e = \frac{(C_0 - C_t)V}{m} \quad (2)$$

Where C_0 is the initial concentration of Cr(VI) in the solution (mg/L), C_t is the concentration of Cr(VI) at a given time (mg/L), m is the mass of the adsorbent (g), and V is the total volume of the Cr(VI) solution (L).

Results and discussion

Initial characterisation of the samples was by XRD. XRD patterns of all the four samples (S1 to S4 as listed in Table 1), shown in Fig. 1, can be indexed to the hexagonal hematite structure (α -Fe₂O₃, JCPDS 33-0664) with unit cell parameters $a = 0.5035$ nm and $c = 1.374$ nm, indicating a good crystallinity of the samples. In the XRD patterns of samples S3 and S4, a few

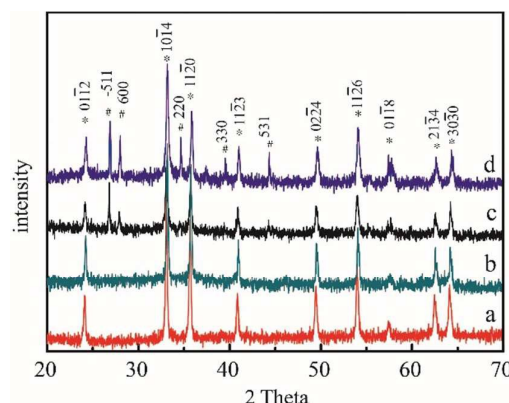


Fig. 1. XRD patterns of the α -Fe₂O₃ nanoparticles with different morphologies, (a) hollow sphere of sample S1, (b) nanotube of sample S2, (c) hollow plate of sample S3, (d) nanoring of sample S4. The peaks in (d) are indexed to α -Fe₂O₃ (*) and Fe₄(PO₄)₃(OH)₃ (#), respectively.

extra weak peaks are indexed to the unit cell of Fe₄(PO₄)₃(OH)₃, with $a = 1.9554$ nm, $b = 0.7395$ nm, $c = 0.7439$ nm, space group C2/c15, (PDF:42-0429).

The particle size and morphology were examined using SEM (Fig. 2). When the concentration of urea was 0.5 mmol/L without adding H₂PO₄⁻ for sample S1, the particle morphology was hollow sphere and the diameter was in a range from 100 to 200 nm (Fig. 2a). As the concentrations of both H₂PO₄⁻ and urea were 1.0 mmol/L, the morphology of the α -Fe₂O₃ particles in sample S2 was nanotube with the length of about 300 nm and the diameter of about 80 nm (Fig. 2b). When the concentrations of H₂PO₄⁻ and urea were increased to 2.5 mmol/L, the produced α -Fe₂O₃ particles in sample S3 had a shape of hollow plate with about 150 nm in diameter and 50 nm in thickness. There is a hole in the face centre of each particle (Fig. 2c). As the concentrations of H₂PO₄⁻ and urea were further increased to 4.0 mmol/L, the morphology of the particles in sample S4 appeared as nanorings (Fig. 2d) with the similar radius to the hollow plates in sample S3. But the particles in sample S4 are

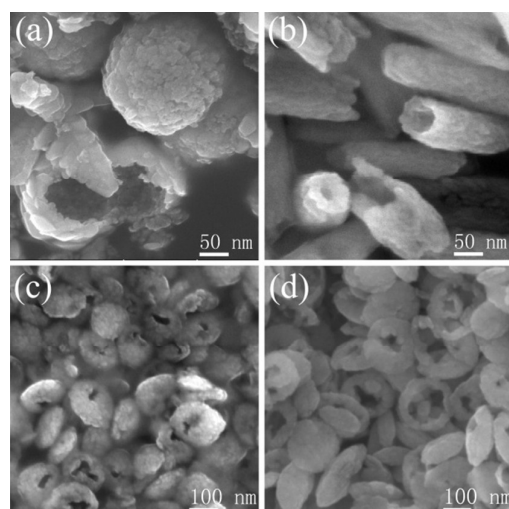


Fig. 2. SEM images of the hematite particles, (a) hollow spheres of S1, (b) nanotubes of S2, (c) nanoplates of S3, and (d) nanorings of S4.

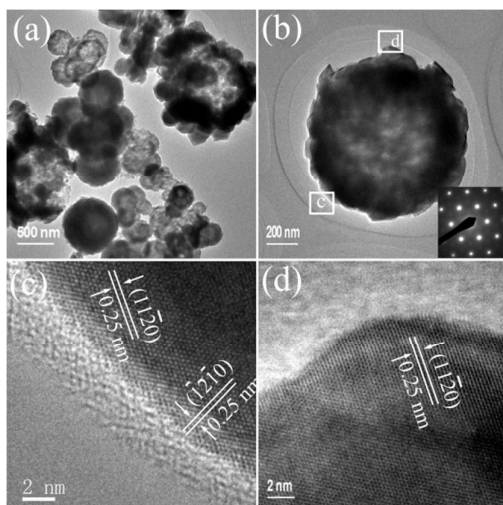


Fig. 3. TEM analysis of the hollow spheres in S1. (a) Low magnification TEM image. (b) TEM image of a single hollow sphere with the corresponding SAED pattern. (c), (d) HRTEM images recorded from the two marked areas in (b).

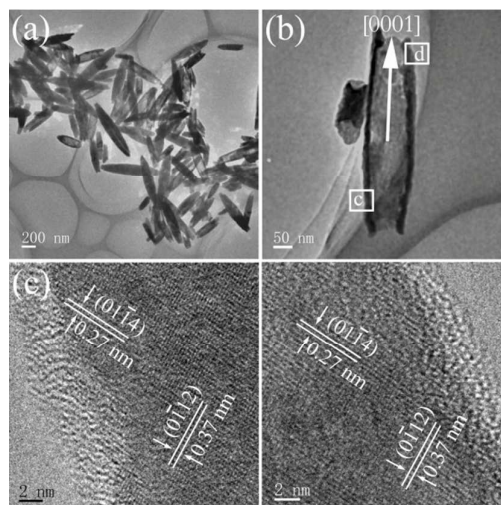


Fig. 4. TEM investigation of the nanotubes in S2. (a) Low magnification TEM image. (b) High magnification TEM image of a single nanotube. (c),(d) HRTEM images of the marked areas in (b).

much thinner than those in sample S3, and the holes in the face centre are bigger. Actually, the hollow plates and nanorings are closely related. The hollow plates must form first and the holes at the face centre are developed later. When the holes become large enough, the particles look like nanorings. Fig. S1 in Electronic Supplementary Information (ESI†) presents low magnification SEM images of these samples, showing the uniformity of the particle morphology and size.

The microstructures of these hematite particles were investigated by using HRTEM. Fig. 3(a) and 3(b) show the spherical particles of sample S1. The light image contrast in the centre indicates their hollow property. Also from the image contrast, the particle seems to be polycrystalline consisting of many nanocrystallites. On the other hand, the corresponding selected area electron diffraction (SAED) pattern in Fig. 3(b) from the whole particle shows a single crystal like diffraction pattern. A possible explanation is that all the nanocrystallites in the particle are self-orientated. Fig. 3(c) and (d) are HRTEM images from two selected top and bottom edge areas. The two d-spacings measured from each image are about 0.25 nm with an interplane angle of 60°, which can be indexed to the $(1\bar{1}\bar{2}0)$ and $(\bar{1}2\bar{1}0)$ planes of the hematite structure. The marked planes in these two HRTEM images are parallel each other, supporting the self-orientated structure.

Fig. 4 shows TEM and HRTEM images of particles in sample S2. The mono-dispersed nanotubes have a shape of weaving shuttle with dimensions of 100 to 200 nm in diameter and 300 to 600 nm in length (Fig. 4a). The wall thickness of about 30 nm is almost uniform, therefore, the inner diameter as well as external diameter at both ends is smaller than that in the middle (Fig. 4b). This shape with non-uniform diameters is different from commonly seen nanotubes with a uniform diameter, such as carbon nanotubes, anodic TiO_2 nanotubes,¹¹ and crystalline titanate and niobate nanotubes.^{12,13} On the other hand, the HRTEM images from the wall of the nanotubes

confirm the hematite crystal structure. The observed d-spacings on Figs. 4(c) and 4(d), 0.27 and 0.37 nm, can be indexed to the $(01\bar{1}4)$ and $(0\bar{1}12)$ with the interplane of 95.6°. Comparing the crystal orientations of the two HRTEM images, we also found that they are well orientated, indicating that the nanotubes can be regarded as porous single crystals. Although determination of crystal orientation along the long axis of the nanotubes is not simple, we are often unable to make sure whether the long axis is perpendicular to the electron beam.¹⁴ For an individual nanotube lying down on the carbon film, it is easy to approach to this position, where the observed orientation along the long axis on the projected image in Fig. 4(b) is parallel to the long axis of the nanotube. This direction can be derived from the marked planes of $(01\bar{1}4)$ and $(0\bar{1}12)$ to be [0001].

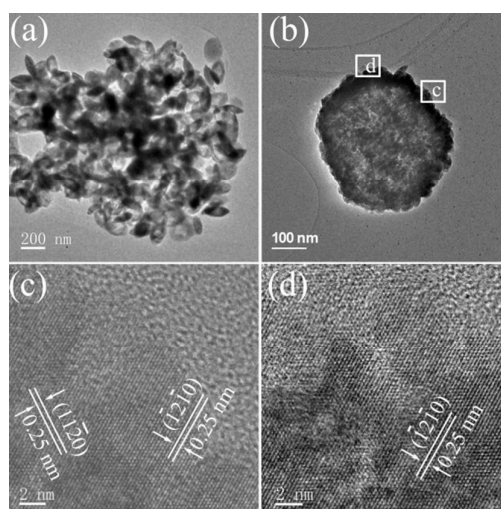


Fig. 5. TEM investigation of the nanoplates in sample S3. (a) Low magnification TEM image. (b) Higher magnification TEM image of a single plate particle. (c), (d) HRTEM images obtained from the two marked areas in (b).

ARTICLE

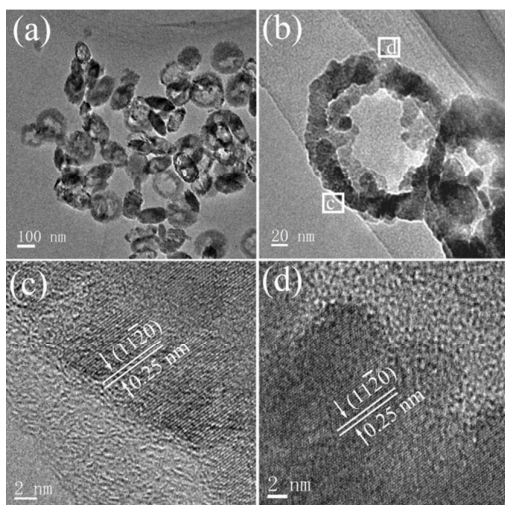


Fig. 6. TEM investigation of nanoring in sample S4. (a) Low magnification TEM image. (b) Higher magnification TEM image of a single nanoring particle. (c), (d) HRTEM images obtained from the two marked areas in (b).

Although the nanoplate morphology of the particles in sample S3 is different from the spherical particles in sample S1, the appearance of microstructures of these two samples on the TEM images are very similar. The HRTEM images of the nanoplates (Fig. 5c and 5d) also show self-orientated aggregation of nanocrystallites, and this orientation extends to the whole particle. The observed d-spacings of 0.25 nm can be indexed to $\{11\bar{2}0\}$ equivalent planes. That means the view direction parallel to the short axis of the nanoplate in Fig. 5(b) is along the [0001] zone axis of the hematite crystal structure.

Fig. 6 shows TEM and HRTEM images of nanoring particles in sample S4. The particle size of ~ 150 nm in diameter and ~ 50 nm in thickness (Fig. 6a) is similar to the hollow plates in sample S3, but much smaller than the spheres in sample S1. It is obvious that the rings consist of many nanocrystallites. But these nanocrystallites connected each other and self-orientated to insure a certain mechanical strength. Viewing along the thickness direction, some d-spacings of 0.25 nm, corresponding to the $\{11\bar{2}0\}$ planes, can be observed on the HRTEM images (Fig. 6c and 6d). The view direction for the particle in Fig. 6b is along the [0001] zone axis, same as the nanoplates in Fig. 5.

In order to identify the influence of NaH_2PO_4 on the morphology formation of hematite crystals, several syntheses with different amounts of NaH_2PO_4 and zero concentration of urea were performed while keeping other parameters constant (Fig. 7). Without the addition of NaH_2PO_4 , relatively large round particles were produced (Fig. 7a). When 1.0 mmol/L NaH_2PO_4 was added to the synthetic solution, the produced particles were spindle-like with an average length of 200 nm and a mean diameter of 50 nm (Fig. 7b). With increasing the concentration of NaH_2PO_4 to 2.5 mmol/L, the morphology of the particles changed to round disk (Fig. 7c). When the NaH_2PO_4 concentration was further increased to 4.0 mmol/L, the disk shape was reproduced, but the thickness of these disks was significantly reduced (Fig. 7d). As the concentration of

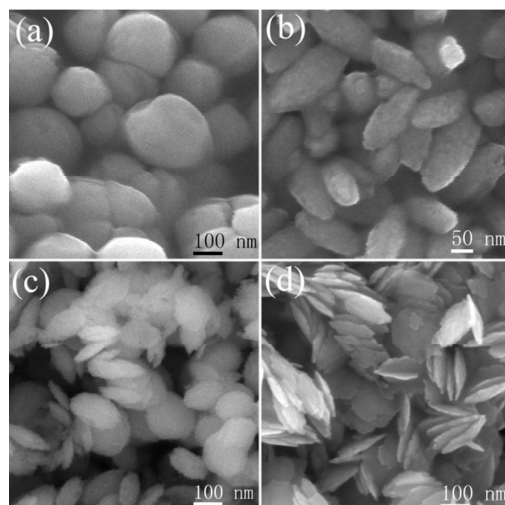


Fig. 7. SEM images of the products prepared with different initial concentrations of NaH_2PO_4 without adding urea, (a) 0, (b) 1.0, (c) 2.5 and (d) 4.0 mmol/L.

NaH_2PO_4 increased to 8 mmol/L (Fig. S2 in ESI†), the $\alpha\text{-Fe}_2\text{O}_3$ particles mainly keep the disk shape, but the size and the thickness are consequently reduced. XPS of the particles obtained in 4.0 mmol/L NaH_2PO_4 without urea (Fig. S3 in ESI†) shows a peak at binding energy of 133.47 eV for P 2p together with peaks from Fe, O, and C. The above results imply that the particles are composite containing phosphate anions and NaH_2PO_4 plays a key role in determining the particle morphology. The four morphologies presented in Fig. 7 have a high degree of similarity with the morphologies in Fig. 2, and can be regarded as templates for the latter. On the other hand, the influence of urea on growth of hollow $\alpha\text{-Fe}_2\text{O}_3$ crystals has been investigated in a similar synthetic system containing FeCl_3 , glucose, and urea.¹⁵ It was found that, even without addition of urea, hollow particles still formed. However, according to the observation in the present work, urea can certainly enhance the formation of hollow particles by gas-bubble-assisted effect.¹⁶

XPS was also carried out on some typical nanoring particles (Fig. 8). The binding energies are corrected for specimen charging by referencing the C 1s line to 284.8 eV. The spectrum reveals that the nanoring surface is mainly composed

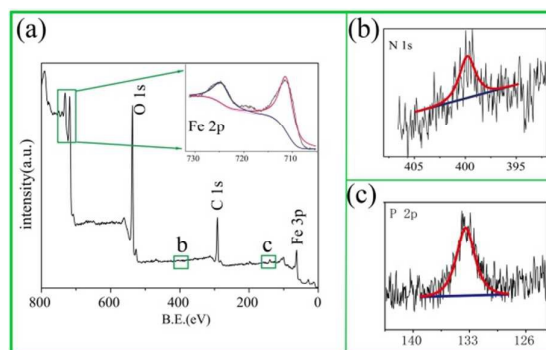


Fig. 8. (a) XPS spectrum of $\alpha\text{-Fe}_2\text{O}_3$ nanorings. (b) high-resolution spectrum of the N 1s and (c) P 2p region.

of Fe and O (Fig. 8a). However, there is a small peak at 399.47 eV for N 1s (Fig. 8b), indicating that there is a small amount of N on the surface of nanorings corresponding to urea deposition. At the same time, a peak at binding energy of 133.47 eV for P 2p is also observed, which could be attributed to the surface adsorbed phosphate anions (Fig. 8c).¹⁷

Based on the above experimental results, it can be concluded that the morphology evolution of α -Fe₂O₃ nanoparticles should be attributed to the co-effect of urea and H₂PO₄⁻. Especially the H₂PO₄⁻ concentration has a great influence on the morphology of the α -Fe₂O₃ nanoparticles. When 0.5 mmol/L of urea was used without adding H₂PO₄⁻, a large number of primary particles precipitated from the solution. Due to their high surface energy, these primary particles were unstable and tended to aggregate into thermodynamically more stable large spheres. With urea decomposing into carbon dioxide and ammonia, a lot of bubbles were gradually generated and the pH value of the solution increased, promoting the nucleation process of α -Fe₂O₃ on the particle surface. As a result, sample S1 with hollow spheres was obtained.

In a solution with 1.0 mmol/L of H₂PO₄⁻ and urea, the amount of H₂PO₄⁻ was rather low compared with the initially formed α -Fe₂O₃ nuclei. The surface hydroxyl configuration on the {0001} facets of α -Fe₂O₃ were all neutral doubly coordinated, but on other normal low-index facets such as the {1010}, {1120}, {0112} and {1014} facets, triply-coordinated surface hydroxyl groups with positive charge exposed the crystal facets. Thus, the adsorption capacities and affinities for phosphate to α -Fe₂O₃ were much lower for the {0001} facets,^{18,19} and then the [0001] direction would grow faster than the other facets, and the spindle-like α -Fe₂O₃ was obtained (Fig. 7b).

The situation was totally different as the concentration of H₂PO₄⁻ increased to 2.5 mmol/L, where nanodisks appeared instead of the spindle particles (Fig. 7c), and the {0001} facets were the main exposed crystal facets. In the reaction system, two kinds of ions (Fe³⁺ and H₂PO₄⁻) could be adsorbed or coordinated with the surface hydroxyls. The adsorption of Fe³⁺ ions favoured the growth of α -Fe₂O₃, but the coordination of H₂PO₄⁻ restrained the growth process. An increase in the concentration of H₂PO₄⁻ ions would induce the intense protonation of the surface hydroxyl groups, and the adsorption of H₂PO₄⁻ on the {0001} facets was enhanced, but the

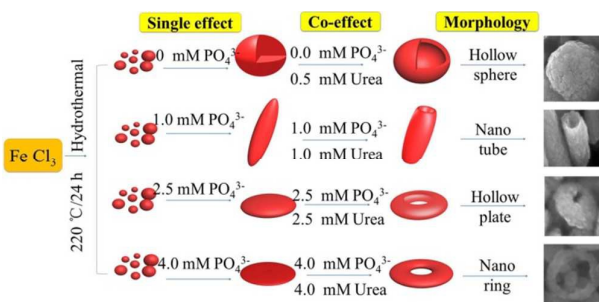
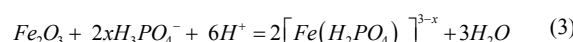


Fig. 9. Sketch of the morphology evolution of α -Fe₂O₃ nanoparticles under the influence of H₂PO₄⁻ ions and urea in 24 h.

adsorption of Fe³⁺ ions was weakened due to the effect of electrostatic attraction. All the special doubly coordinated hydroxyl groups on the {0001} facets did not facilitate the adsorption of H₂PO₄⁻ ions. As a result, nanodisks with the exposed {0001} facets were obtained due to a slower growth of the {0001} facets in comparison with the other facets (Fig. 7d). Finally, the excess H₂PO₄⁻ had a dissolution effect on the α -Fe₂O₃ surface follow the eqn (3):¹⁸



This dissolution process mainly occurred on the {0001} facets due to the fact that the {0001} facets had the highest concentration of exposed Fe³⁺ ions and the second among the normal low-index facets.^{20,21} with single effect of H₂PO₄⁻, this dissolution process will happen if the time of hydrothermal reaction reached 48 h.^{18,21} According to Zhang *et.al.*, the thickness of the α -Fe₂O₃ barrels can be controlled to some extent by adjusting the amount of urea with its gas-bubble-assisted effect.^{15,22} The hollow structure and rough surface can also form with this effect. With the help of this effect, the dissolution process along the [0001] direction could be achieved in 24 h, leading to the holes formation in samples S2-S4. The intensity of the peaks (511) and (600) of Fe₄(PO₄)₃(OH)₃ obviously increased in the XRD patterns of samples S3 and S4 (Fig. 1), which could be regarded as another

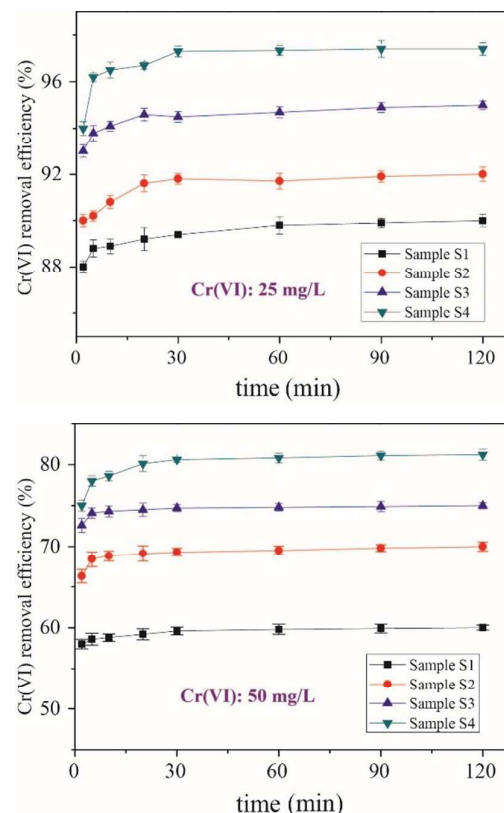


Fig. 10. Adsorption kinetic of different Cr(VI) concentrations on the as-prepared α -Fe₂O₃; (a) 25 mg/L, (b) 50 mg/L. (Adsorbent dosage: 2.4 g/L, no pH adjustment, shaking speed: 150 rpm, T:25°C).

ARTICLE

evidence for the dissolution process. The formation routes of the different morphologies of $\alpha\text{-Fe}_2\text{O}_3$ are illustrated in Fig. 9.

Fig. 10 shows the Cr(VI) removal efficiency by 2.4 g/L as-prepared $\alpha\text{-Fe}_2\text{O}_3$ with two initial Cr(VI) concentrations (25 mg/L and 50 mg/L). It is observed that the Cr(VI) adsorption can reach to equilibrium within the first half an hour. Therefore, Cr(VI) can easily access to the surface of the well-dispersed $\alpha\text{-Fe}_2\text{O}_3$ nanoparticles. At the concentration of 25 mg/L (Fig. 10a), the Cr(VI) removal efficiency is up to 97.4% by nanorings in sample S4. The hollow spheres in sample S1 have the lowest removal efficiency (90%). The removal efficiency is decreased when the concentration Cr(VI) increases to 50 mg/L (Fig. 10b). Although the Cr(VI) removal efficiency by nanorings decreases to 81.2% in the latter case, the adsorption capacity can still reach to 16.9 mg/g, that is higher than other $\alpha\text{-Fe}_2\text{O}_3$ nanoparticles.⁵ In comparison with previous reports (Table S1 in ESI†), the nanorings (sample S4) have very high level capacity of the Cr(VI) removal (16.9 mg/g) among the non-porous $\alpha\text{-Fe}_2\text{O}_3$ materials.

The difference in Cr(VI) removal efficiency among the four samples prepared in the present work is mainly attributed to the different surface areas and exposed surface planes. Because the adsorption occurs on the particle surface, a higher surface area will have a higher adsorption capacity. The surface areas of these $\alpha\text{-Fe}_2\text{O}_3$ particles are 31.1 m²/g (sample S1), 34.2 m²/g (sample S2), 38.5 m²/g (sample S3), and 36.7 m²/g (sample S4). The difference is not significant. On the other hand, the Cr(VI) removal efficiency also depends on the type of exposed crystallographic planes. The more the {0001} planes exposed, the high the adsorption capacity.

Furthermore, pH value of the solution has also an influence on removal of Cr(VI). In this study, this effect of the four different $\alpha\text{-Fe}_2\text{O}_3$ samples was investigated by changing the initial pH from 3 to 11 and the results are shown in Fig. 11. The equilibrium adsorption capacities are reduced with pH increased. As the pH value increases to 11, the adsorption capacity is decreased to 14.7 mg/g. This phenomenon can be understood as the low pH value in the solution would leave higher concentration of positively charged hydroxyl groups on the $\alpha\text{-Fe}_2\text{O}_3$ surface, which has a larger power to attract the CrO_4^{2-} anions.

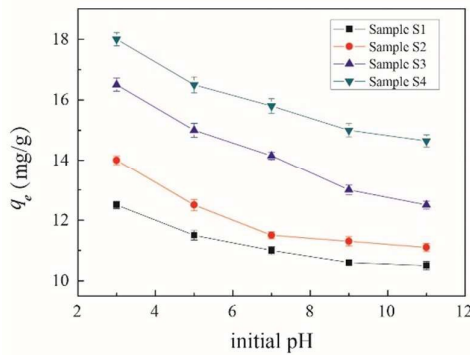


Fig. 11. Effect of initial pH on the removal of Cr(VI). (Adsorbent dosage: 2.4 g/L, Cr(VI) concentration: 50 mg/L, shaking speed: 120 rpm, contact time: 150 min, T:25 °C.)

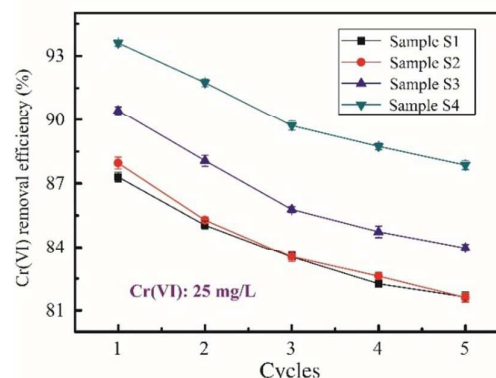


Fig. 12. 5th consecutive Recycled Cr(VI) removal efficiency of as-prepared Samples S1-S4.

Desorption is another important process reflecting the economical and enhancement values of the adsorption. In this study, the removal efficiencies of the regenerated $\alpha\text{-Fe}_2\text{O}_3$ nanoparticles are shown in Fig. 12. The results indicate that the adsorption capability decrease gradually in first three cycles and then decrease with increase of cycles at a relatively slower rate. The nanorings in sample S4 has high removal ability without loss of much efficiency after 5 cycles. The results may be related to the higher proportion of outer surface of the nanorings in sample S4 than samples S2 and S3. The regeneration process needs more outer surface area, pore and channel for the desorption of Cr(VI). Nevertheless, all the four samples of $\alpha\text{-Fe}_2\text{O}_3$ can be reused for removal of Cr(VI) and can make the overall process cost effective.

From the adsorption results in the systems with different pH values and different morphologies of $\alpha\text{-Fe}_2\text{O}_3$, the adsorption mechanism may be deduced to be chemical adsorption at the doubly and triply coordinated hydroxyl groups on the $\alpha\text{-Fe}_2\text{O}_3$ surface. Because these two types of hydroxyl groups are in neutral and positive overall charging states, they can adsorb CrO_4^{2-} ions by electrostatic attraction. Different planes in $\alpha\text{-Fe}_2\text{O}_3$ have different densities of these hydroxyl groups. Among the low index planes, the (0001) plane has the highest density of the doubly coordinated hydroxyl groups (13.7 nm^{-2}) in comparison with the (1010) and (1120) planes (2.9 nm^{-2} , 5.0 nm^{-2}).²³ Besides this, the (0001) plane does not have singly

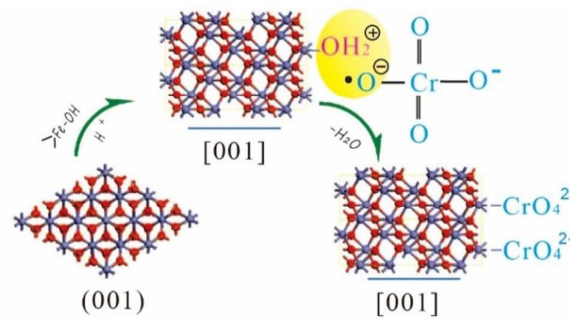


Fig. 13. Possible mechanism of Cr(VI) adsorption on $\alpha\text{-Fe}_2\text{O}_3$.

coordinated hydroxyl with a negative charge. Consequently, the nanoplates in sample S3 and nanorings in S4 with more (0001) planes exposed have high adsorption capacities than the nanospheres in S1 and nanotubes in S2. Because of the open structure of nanorings have a higher surface area than the closed structure of hollow nanoplate, sample S4 removes Cr(VI) more efficiently than S3. The pH value can usually influence the electronic structures of the surface hydroxyl groups. Under an acidic condition, the coordinated hydroxyl groups easily form FeOH^{2+} , which predominate over the surface.²⁴ Therefore, $\alpha\text{-Fe}_2\text{O}_3$ has a high adsorbent capacity at low pH values. The important role of the surface hydroxyl groups in the formation of some novel morphologies, e.g. snowflake-like $\alpha\text{-Fe}_2\text{O}_3$ and 8-branch Cu_2O , have also been reported recently.^{25,26} Consequently, the adsorption mechanism of Cr(VI) species on $\alpha\text{-Fe}_2\text{O}_3$ studied in the present work can be proposed as depicted in Fig. 13.

Conclusion:

The $\alpha\text{-Fe}_2\text{O}_3$ nanoparticle with different morphologies, such as hollow spheres, nanotubes, nanoplates and nanorings, were synthesised by using NaH_2PO_4 and urea via a facile hydrothermal method. These $\alpha\text{-Fe}_2\text{O}_3$ nanoparticles have good dispersion without solid substrates. The adsorption of Cr (VI) results showed that the $\alpha\text{-Fe}_2\text{O}_3$ with nanoring-like morphology has the highest removal efficiency and adsorption capacity. The adsorption mechanism of Cr (VI) onto hematite nanoparticles is chemisorption process through outer surface of doubly and triply coordinated hydroxyl groups.

Acknowledgements

This work was financially supported by the National Nature Science Foundation of China (No: 51302280, 51574286), Natural Science Foundation in Qinghai province (No: 2014-ZJ-936Q), CAS "Light of West China" Program and Youth Innovation Promotion Association (2016377), CAS.

Notes and references

- Y. Mu, Z. H. Ai, L. Z. Zhang and F. H. Song, *Accts Appl. Mater. Inter.*, 2015, **7**, 1997-2005.
- J. P. Beukes, P. G. van Zyl and M. Ras, *J. Southern Afr. Inst. Min. Metall.*, 2012, **112**, 347-352.
- X. Li, R. Zhao, B. L. Sun, X. F. Lu, C. C. Zhang, Z. J. Wang and C. Wang, *RSC Adv.*, 2014, **4**, 42376-42382.
- C. E. Barrera-Diaz, V. Lugo-Lugo and B. Bilyeu, *J. Hazard Mater.*, 2012, **223**, 1-12.
- H. I. Adegoke, F. AmooAdekola, O. S. Fatoki and B. J. Ximba, *Korean J. Chem. Eng.*, 2014, **31**, 142-154.
- C. Y. Cao, J. Qu, W. S. Yan, J. F. Zhu, Z. Y. Wu and W. G. Song, *Langmuir*, 2012, **28**, 4573-4579.
- C. L. Han, J. S. Xie, C. H. Deng and D. F. Zhao, *J. Chil. Chem. Soc.*, 2012, **57**, 1372-1374.
- E. T. Liu, H. P. Zhao, H. Li, G. F. Li, Y. L. Liu and R. Chen, *New J. Chem.*, 2014, **38**, 2911-2916.
- S. X. Yin and D. E. Ellis, *Surf. Sci.*, 2009, **603**, 736-746.
- X. P. Huang, X. J. Hou, F. H. Song, J. C. Zhao and L. Z. Zhang, *Environ. Sci. Technol.*, 2016, **50**, 1964-1972.
- Z. X. Su and W. Z. Zhou, *J. Mater. Chem.*, 2011, **21**, 357-362.
- Q. Chen, W. Z. Zhou, G. H. Du and L. M. Peng, *Adv. Mater.*, 2002, **14**, 1208-1211.
- G. H. Du, Q. Chen, Y. Yu, S. Zhang, W. Z. Zhou and L. M. Peng, *J. Mater. Chem.*, 2004, **14**, 1437-1442.
- W. Z. Zhou and H. F. Greer, *Eur. J. Inorg. Chem.*, 2016, 941-950.
- X. H. Zhang, Y. Z. Chen, H. Liu, Y. Wei and W. Wei, *CrystEngComm*, 2013, **15**, 6184-6190.
- X. Liu, Y. F. Li, W. W. Zhu and P. F. Fu, *CrystEngComm*, 2013, **15**, 4937-4947.
- Z. Liu, B. L. Lv, Y. Xu and D. Wu, *J. Mater. Chem. A*, 2013, **1**, 3040-3046.
- C.-J. Jia, L.-D. Sun, Z.-G. Yan, L.-P. You, F. Luo, X.-D. Han, Y.-C. Pang, Z. Zhang and C.-H. Yan, *Angew. Chem. Int. Ed.*, 2005, **44**, 4328-4333.
- C. J. Jia, L. D. Sun, F. Luo, X. D. Han, L. J. Heyderman, Z. G. Yan, C. H. Yan, K. Zheng, Z. Zhang, M. Takano, N. Hayashi, M. Eltschka, M. Klau, U. Rudiger, T. Kasama, L. Cervera-Gontard, R. E. Dunin-Borkowski, G. Tzvetkov and J. Raabe, *J. Am. Chem. Soc.*, 2008, **130**, 16968-16977.
- B. Lv, Z. Liu, H. Tian, Y. Xu, D. Wu and Y. Sun, *Adv. Funct. Mater.*, 2010, **20**, 3987-3996.
- B. L. Lv, Y. Xu, D. Wu and Y. H. Sun, *CrystEngComm*, 2011, **13**, 7293-7298.
- W. Cheng, K. B. Tang, Y. X. Qi, J. Sheng and Z. P. Liu, *J. Mater. Chem.*, 2010, **20**, 1799-1805.
- R. M. Cornell and U. Schwertman, *The Iron Oxides: Structure, Properties, Reaction, Occurrences and Use.*, Second ed., WILEY-VCH GmbH&Co.KGaA, 2003.
- Z. H. Ruan, J. H. Wu, J. F. Huang, Z. T. Lin, Y. F. Li, Y. L. Liu, P. Y. Cao, Y. P. Fang, J. Xie and G. B. Jiang, *J. Mater. Chem. A*, 2015, **3**, 4595-4603.
- Z. Liu, C.-Y. Chiang, W. Li and W. Z. Zhou, *Chem. Commun.*, 2015, **51**, 9350-9353.
- K. Self and W. Z. Zhou, *Crystal Growth & Design*, 2016, in press. DOI: 10.1021/acs.cgd.6b00883.

$\alpha\text{-Fe}_2\text{O}_3$ nanoparticle with different morphologies, such as hollow spheres, nanotubes with limited {0001} plane exposed, nanoplates and nanorings with the {0001} plane predominantly exposed, have been synthesized by using NaH_2PO_4 and urea in a facile hydrothermal method. As a high efficient Cr(VI) adsorbents of nanorings by (0001) planes exposed, the adsorption mechanism may be due to chemical adsorption by the doubly and triply coordinated hydroxyl groups on $\alpha\text{-Fe}_2\text{O}_3$ surface.

